Unravelling microstructure-electroactivity relationships in free-standing polycrystalline boron-doped diamond

A mapping study

Liu, Zhichao; Baluchová, Simona; Li, Ziyu; Gonzalez-Garcia, Yaiza; Hall, Clive E.; Buijnsters, Josephus G.

DOI
10.1016/j.actamat.2024.119671

Publication date
2024

Document Version
Final published version

Published in
Acta Materialia

Acta Materialia 266 (2024) 119671

Contents lists available at ScienceDirect

Acta Materialia

journal homepage: www.elsevier.com/locate/actamat

Full length article

Unravelling microstructure-electroactivity relationships in free-standing polycrystalline boron-doped diamond: A mapping study

Zhichao Liu [a], Simona Baluchová [a], Ziyu Li [b], Yaiza Gonzalez-Garcia [b], Clive E. Hall [c], Josephus G. Buijnsters [a,*]

[a] Department of Precision and Microsystems Engineering, Delft University of Technology, Mekelweg 2, 2628 CD Delft, the Netherlands
[b] Department of Materials Science and Engineering, Delft University of Technology, Mekelweg 2, 2628 CD Delft, the Netherlands
[c] Mintres BV, De Nieuwe Erven 8, 5431 NT Cuijk, the Netherlands

ARTICLE INFO

Keywords:
Boron-doped diamond (BDD)
Raman mapping
Electron backscatter diffraction
Scanning electrochemical microscopy (SECM)
Grain boundaries

ABSTRACT

In this work, four different techniques were concurrently applied to study the interplay between local electroactivity and electrode surface characteristics of free-standing, polycrystalline boron-doped diamond (BDD). Scanning electron microscopy, electron back-scatter diffraction, Raman mapping and scanning electrochemical microscopy were used to probe the electrode morphology, grain orientation and boundaries, composition, and local electrochemical activity, respectively. Both nucleation and growth BDD surfaces together with the cross-section area were carefully investigated for the first time in a single study using the combination of all four techniques. This enabled us to obtain significant insights into the highly heterogeneous nature of the polycrystalline BDD material. Notably, boron dopants were confirmed to be non-uniformly distributed over the BDD material, which is characterized by a distinct columnar structure and composition of grains of various orientations. Particularly, the highest electrochemical activity was recorded on the highest doped (111) crystal orientation. In contrast, the averagely boron-doped (100)-oriented facet showed non-conductive nature. This highlights that the local electrochemical activity of the BDD surface is strongly grain-dependent and the most significant factors governing the obtained responses are crystallographic orientation and boron doping. Moreover, increased boron and sp^2 carbon content in the boundary regions was recognized by Raman mapping. However, such localized enrichment in impurities did not translate into enhanced electrochemical activity, which implies that boron atoms at the inter-grain areas are predominantly inactive. Finally, it is crucial to consider all characteristics of the polycrystalline BDD including crystal orientation, which is particularly relevant if micro- and nanoscale probing is intended.

1. Introduction

Since its introduction some four decades ago, polycrystalline boron-doped diamond (BDD) has found extensive application in various fields including electroanalysis, development of novel electrochemical (bio) sensors [1,2] and electrochemiluminescence systems [3], water treatment processes and mineralization of pollutants [4–6], electrosynthesis [7], electrocatalysis [8], and electrochemical energy storage [9]. Such wide spread of the BDD-based electrodes can be ascribed to their sp^3-hybridized carbon nature resulting in exceptional properties such as superior chemical and mechanical stability, wide potential window, low capacitive and background currents, reduced susceptibility towards corrosion and (bio)fouling, and biocompatibility [1,10–12]. Moreover, BDD electrodes possess an adjustable electrical conductivity [13,14] and surface termination [15,16], representing two key material properties with major influence on electrode performance and applicability. Other parameters affecting the BDD characteristics are the fraction of grain boundaries with associated content of non-diamond (sp^2) carbon [13,17,18], surface finish [17,19,20] and crystallographic orientation [15,21,22].

In principle, all factors listed above are governed by conditions defined during the chemical vapour deposition (CVD) process that is typically used for the BDD synthesis. Boron doping is accomplished from the gas phase by adding a boron-containing compound, such as diborane, trimethyl borane, trimethyl borate or boron trioxide, into the CVD reaction chamber with the source gases, i.e., carbon-containing gas

* Corresponding author.
E-mail address: J.G.Buijnsters@tudelft.nl (J.G. Buijnsters).

https://doi.org/10.1016/j.actamat.2024.119671
Received 11 October 2023; Received in revised form 1 December 2023; Accepted 9 January 2024
Available online 12 January 2024

(typically methane) and hydrogen [10]. Depending on the boron amount, either semi-conductive or metal-like conductive BDD electrodes can be prepared; a threshold for metallic type conductivity was determined to be $\sim 1-3\times10^{20}$ atoms cm^{-3} [23,24]. Consequently, the boron doping level influences the heterogeneous electron transfer (HET) kinetics at the electrode−electrolyte interface, which is then manifested in the recorded responses (potential positioning and signal intensity) of studied redox-active molecules [13,14].

Notably, boron integrates within the diamond lattice in a non-uniform way. It has been shown that the amount of boron incorporated varies between the differently oriented diamond crystal faces and increases in the following order: (100) < (110) < (111) [25]. Using the same boron-to-carbon ratio in the gas phase during the CVD process results in approximately one order of magnitude higher boron concentration in the (111) surface, compared to the (100) orientation [26,27]. Consequently, boron atoms are heterogeneously distributed across the polycrystalline BDD surfaces, which generates domains of various doping levels and thus conductivity (possibly spanning from insulating to semiconducting to metal-like) and electrochemical activity [28,29]. Recently, Einaga & Takahashi et al. investigated the electrochemical properties of (100) and (111) crystal facets of isolated single BDD microparticles using the nanoscale reactivity mapping technique [30]. The results revealed significantly faster HET kinetics, and thus higher activity, on the (111) facet, compared to the (100) facet and such difference was ascribed to the higher boron dopant density present on the (111)-oriented crystal [30].

Further, the CVD process is of non-equilibrium nature, which results in the formation of various structural defects, such as twinned crystal domains with corresponding twin boundaries [31,32]. Via the formation of twin boundaries, the diamond lattice effectively manages accumulated stress created by the incorporation of impurities (boron dopant) during the CVD growth [32]. Notably, (111) orientations are prone to easily formed twinning and defects [33], which is in contrast to (100) faces typically containing fewer structural defect sites [34]. Several researchers have claimed preferential accumulation of boron dopant at such defective sites and at twin, or in general, grain boundaries [32,35,36]. Others, though, have reported no enhanced boron doping at the inter-grain regions [37], which also serve as sites for the enrichment of sp^2 carbon impurities possessing electrocatalytic activity [38]. These factors undoubtedly contribute to significant non-uniformity across the polycrystalline BDD electrode surfaces. Evidently, surface heterogeneities considerably influence the concentration and mobility of charge carriers at the BDD electrode surface and their effect is often manifested by differences in electrochemical activity.

Several attempts have been made to address BDD heterogeneity using a range of techniques including electrogenerated chemiluminescence [39], cathodoluminescence [29], photoluminescence and micro-secondary-ion mass spectrometry [40], scanning transmission electron microscopy and electron energy-loss spectroscopy [32], Raman spectroscopy and imaging [35,37], scanning electrochemical microscopy (SECM) [28,29,38], conductive atomic force microscopy (AFM) [29,38], and impedance imaging [36,41]. However, contradictory results and conclusions have been reported in the literature: Bard et al. [38] investigated differently doped polycrystalline BDD electrodes ([B] ranging from 2×10^{17} to 2×10^{20} atoms cm^{-3}) using conductive AFM and SECM and claimed that their surfaces are predominantly insulating with non-uniformly distributed conducting areas creating “hot spots” of electrochemical activity. Also, grain boundaries were identified as high conductivity regions, where boron atoms are possibly accumulated [38], which agrees with the findings acquired by local impedance imaging presented in [36]. In contrast, works by Macpherson & Unwin et al. [28,29,42] indicated that the entire surface of highly doped ($\sim5\times10^{20}$ atoms cm^{-3}) polycrystalline BDD electrodes is electrochemically active, however, the local heterogeneities in electroactivity (more vs. less conducting regions) were identified and correlated with the facet-dependent variations in boron doping level. This was concluded from SECM-based surface analyses which also did not reveal any enhanced conductivity nor increased electroactivity at grain boundaries [28,29,42].

Apparently, unravelling direct and conclusive links between particular variations in BDD surface characteristics and localized electrochemical activity continues to be a challenge. Therefore, this work aims to gain deeper understanding on the heterogeneity of self-supported, polycrystalline BDD electrodes. They possess, in general, so-called nucleation and growth surfaces, which can be either in their “as-deposited” or polished state. Previously, we have demonstrated how nucleation, growth and polished growth surfaces of such electrodes vary in crystalline size, and content of boron dopant and sp^2 carbon sites, which also translates into different electrochemical behaviour towards the sensing of glucose [17]. In this work, the polished nucleation and growth surfaces as well as the cross-section area of the free-standing, polycrystalline BDD material were subjected to thorough investigation using several techniques. Scanning electron microscopy (SEM) was used to analyze the morphological characteristics and electron back-scatter diffraction (EBSD) was applied to create orientation and boundary maps of the individual electrode regions, which allowed for the confirmation and quantification of primary and secondary twins. Raman spectroscopic imaging was employed to map the distribution of sp^3 (diamond) and sp^2 (non-diamond) carbon as well as boron dopants throughout the different BDD surfaces. Moreover, the polished growth surface of the BDD electrode, the most commonly employed in electrochemical studies, was subjected to SECM mapping experiments to probe its conductive and electrochemically active areas using an outer-sphere ferrocenemethanol ($FcMeOH^{+/0}$) redox couple. The exclusive combination of EBSD, Raman and SECM mapping, performed on a single electrode, allowed to illuminate the interplay between local electrochemical activity and investigated surface characteristics, including crystal orientation, grain (twin) boundaries, boron doping, and carbon phase composition.

2. Experimental

2.1. Preparation of free-standing BDD electrodes

Two free-standing ~700 μm thick BDD electrodes with a boron content of $\sim3\times10^{20}$ cm^{-3} and a resistivity of 0.50 mΩ m were sourced from Diafilm EP Grade BDD (Element Six, UK) and acquired from Mintres B.V. (The Netherlands). Both BDD samples were grown using a commercial microwave plasma CVD process, developed in-house. The growth and nucleation surfaces of the first BDD electrode (1.5×1.5 cm^2) were mechanically polished until a surface mean roughness of <10 nm was achieved. In the case of the second BDD electrode (1.0×0.5 cm^2), resulting from the fragmentation of a larger sample, only the cross-sectional area was chem-mechanically polished and analyzed, while its growth and nucleation surfaces were preserved in “as-deposited” state and were not exposed to any measurements.

Prior to use, both studied BDD samples were firstly ultrasonicated in acetone, isopropanol, and deionized water (5 min in each medium) and subsequently acid cleaned by boiling for 5 min in a mixture composed of concentrated HCl, H_2SO_4, and HNO_3 in a ratio of 2:2:3, which resulted in clean and stable oxygen-terminated surfaces. Finally, the electrodes were extensively rinsed with deionized water and dried with compressed air.

To ensure performing various measurements (SEM, EBSD, Raman and SECM mapping) on the same location within the polished growth BDD surface and to enable their correlation, a reference cross with lines of ~30 μm in width was laser cut on the sample.

2.2. Microscopic and spectroscopic measurements

The surface morphology, crystal orientation, and grain boundary information of the processed BDD electrodes were acquired using an SEM operating at a 15 kV accelerating voltage (JEOL JSM6500F, Japan) and equipped with an EBSD detector (Helios G4 PFIB UXe, Thermo Fisher Scientific, USA). EBSD orientation maps were created using the OIM Analysis software (EDAX, USA), which evaluated the recorded Kikuchi diffraction patterns. The grain boundaries were identified as regions where the angular misorientation between two contiguous crystalline grains exceeds 2°. In addition, primary and secondary twinning boundaries were classified based on the distinct crystallographic parameters. Specifically, primary twinning boundaries exhibit a misorientation defined by a <111> rotational axis coupled with an angular deviation ranging from 58° to 62°. In contrast, secondary twinning boundaries are identified by a ⟨110⟩ rotational axis with an associated misorientation angle spanning from 36.9° to 40.9° [43]. X-ray diffraction (XRD) analysis was performed using a Bruker D8 Advance diffractometer with a Bragg-Brentano geometry and a Lynxeye XE position sensitive detector using CuKα radiation. Surface roughness was determined from AFM measurements with a JPK Nanowizard 4 (Bruker, USA) in a tapping mode with silicon tips over a scanned area of 100 × 100 μm^2. Raman spectra were acquired with a Horiba LabRAM HR (Japan) device equipped with a solid state Cobolt FandangoTM laser operating at 515 nm wavelength (Hübner Photonics, Germany). Raman imaging was performed using a 100× objective with a spot size of ~300 nm and a step size of 1 μm; during the surface mapping, the full spectra in the range from 200 to 1800 cm^{-1} for each point were recorded and stored. As-recorded Raman spectra were used without any background correction to compose Raman intensity maps corresponding to the dominant spectral features. Particularly, the width and the intensity of the peak located at ~1330 cm^{-1} and the band intensity at ~1550 cm^{-1} were evaluated and employed for Raman imaging.

2.3. Electrochemical measurements

Cyclic voltammograms of $FcMeOH^{+/0}$ redox probe were recorded on the polished growth surface of the polycrystalline BDD working electrode, placed in a lab-made PTFE cell, using an Autolab PGSTAT 128 N controlled by Nova 2.1 software (Metrohm, The Netherlands). A conventional three-electrode configuration was completed with a platinum counter electrode (5.7 cm long wire) and a silver-silver chloride reference electrode (both ALS Co, Japan).

SECM measurements were performed using a Scanning Electrochemical Workstation Model 370 (Ametek Scientific Instruments, USA). A Pt microelectrode probe, sealed in a glass tube, with a 10 μm diameter tip was employed as a working electrode; the ratio of the radius of the insulating glass sheath to the radius of the Pt disk (RG) was 5. The cell was completed with a reference Ag/AgCl (3 M KCl) electrode and a Pt wire serving as the counter electrode. The SECM was operated under feedback mode using 1 mM $FcMeOH^{+/0}$ (in 0.1 M KNO_3) as a redox mediator. The redox potential of +0.5 V, selected based on cyclic voltammograms recorded with the same set-up, was applied at the Pt electrode to oxidize this mediator, while the BDD electrode was kept under open circuit potential (OCP). The SECM map of the polished growth BDD surface was recorded in an area of 100 × 80 μm^2 with a scanning rate of 2 μm s^{-1} and a tip-substrate distance fixed to 2 μm. Besides, approach curves were recorded to probe the electrochemical nature of the individual spots (six in total) located at the polished growth BDD surface, i.e., to identify whether they are active or inactive. The Pt probe tip carefully approached to the substrate (BDD) in the feedback mode at a rate of 0.1 μm s^{-1}. Curves were displayed using normalised current (I) and distance (L). I corresponds to the ratio between the measured probe current (i_T) and the steady-state current (i_{ss}) recorded far from the substrate. L represents the ratio between substrate-to-probe tip distance (d) and the tip radius (r). All cyclic voltammetry (CV) and SECM measurements were conducted at room temperature (23 ± 1 °C).

2.4. Chemicals

Ferrocenemethanol (97 %), potassium nitrite (≥99 %), sulphuric acid (95 – 98 %), hydrochloric acid (37 %), nitric acid (70 %), isopropanol, and acetone were purchased from Merck and used as-received. Deionized water (resulting resistivity of >18.0 MΩ cm), purified with a LWTN Genie A system (Laboratorium Water Technologie Nederland), was used to prepare all aqueous solutions.

3. Results and discussion

3.1. SEM and EBSD analysis

The morphological characteristics of the polycrystalline BDD samples were observed using SEM, whereas crystal orientation and grain boundary maps were imaged based on the EBSD measurements. The cross-section area of the BDD material was probed and is depicted in Fig. 1. The nucleation side consisting of smaller grains is visualized at the bottom of the images. As the images progress to the top, larger crystals can be clearly identified. The columnar structure typical for the CVD diamond growth was visualized by SEM (Fig. 1(A)), while EBSD mapping revealed a rich mixture of crystal orientations (Fig. 1(B)). Grains either possessing or leaning toward (100), (110) and (111) orientations are clearly observed in Fig. 1(B) across the entire sample cross-section area. No preferential development of a specific orientation along the growth direction (i.e., from nucleation toward growth surface) can be distinguished. Further, the boundary map displayed in Fig. 1(C) shows a significant number of grain boundaries (marked as black lines) as well as primary and secondary twin boundaries (in red and green colour, respectively) whose quantity was estimated to be 19 % and 12 %, respectively. Such twinning operations are a typical feature of columnar crystal growth of the polycrystalline diamond.

The same coupled SEM/EBSD analysis was conducted on the polished nucleation and growth surfaces of the BDD material; the obtained micrographs and maps are visualized in Fig. 2. The SEM images clearly show that the growth surface consists of crystals of different dimensions including relatively large grains up to several tens of microns in diameter, while on average smaller grains down to ~1 μm are identified on the nucleation surface. This is further supported by the histograms provided in Fig. 3, which show the distribution of the diamond grain sizes within the individual surfaces. The growth side includes grains whose diameter widely ranges between 4 and 53 μm, whereas the grain size range is narrower on the nucleation surface, where the largest crystals do not exceed 10 μm in diameter. As can be further derived from the dashed fitting curves in Fig. 3(A, C), the most prevailing grain size on the growth and nucleation BDD surface is located at ~26 μm and ~6 μm, respectively.

The EBSD orientation maps (Fig. 2(B, E)) demonstrate that the majority of both growth and nucleation surfaces consist of (110) orientation with a small contribution from (100) and (111) to the overall surface textures. This is presumably related to the fact that ⟨110⟩ is the direction of the fastest growth [44]. Similarly, previous works also reported on the dominance of (110) orientation over (100) and (111) in polycrystalline (doped) diamond, in the form of both a thin film (thickness of ≤0.5 μm) [20] and a free-standing electrode (thickness of several hundred μm) [44,45]. Besides, EBSD enabled to visualize the boundary maps for the polished growth and nucleation surfaces (Fig. 2 (C, F)); the latter contains much more grain boundaries due to the smaller grain sizes, where sp^2-hybridized carbon typically resides [17, 46]. Primary and secondary twins between the crystallites on the

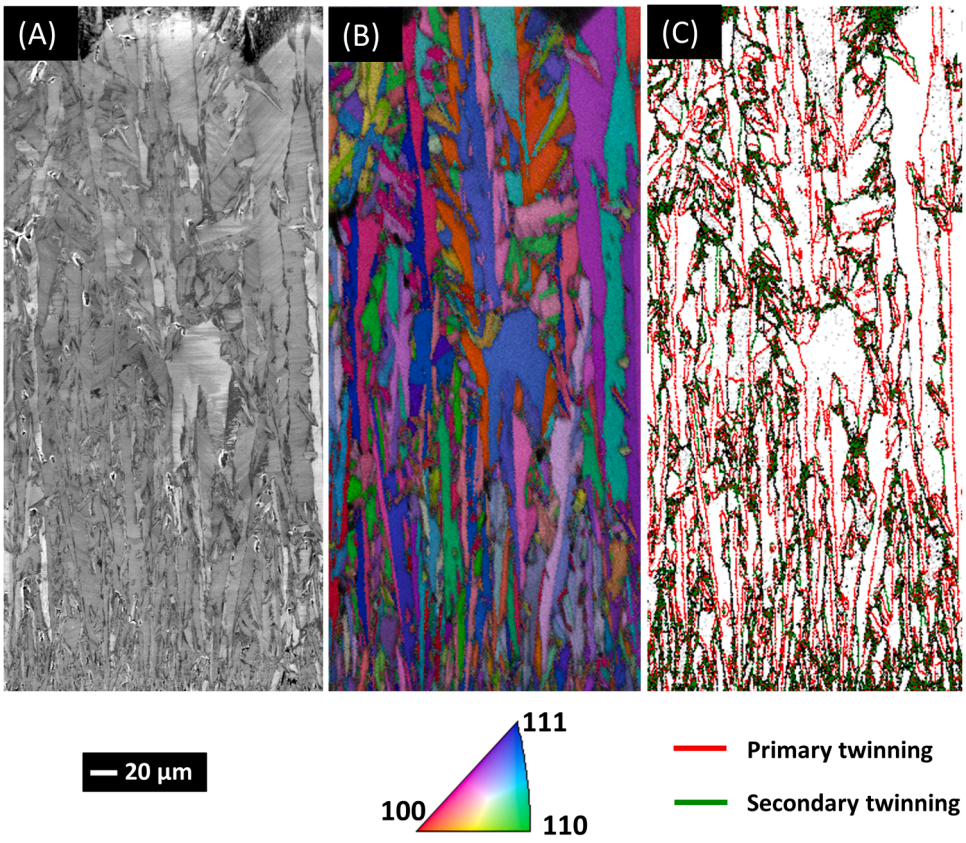

Fig. 1. (A) SEM image, (B) EBSD map visualizing crystalline orientation, and (C) grain boundary map acquired from the cross-section of the free-standing, polycrystalline BDD electrode.

nucleation surface represent a fraction of 29 % and 14 % of all grain boundaries, respectively. In contrast, higher fraction of primary twin boundaries, i.e., 44 %, was found on the polished growth side (Fig. 2(C)), however, the secondary twins occur with a similar incidence of 13 %. Noticeably, thicker and darker grain boundaries recognized in the SEM image of the growth surface were identified as primary twins in the boundary map (marked by red arrows in Fig. 2(C)), while thinner and lighter boundaries appeared as 'regular' grain boundaries (marked by black arrows in Fig. 2(C)).

Further, the recorded XRD patterns, shown in Fig. S1(A, B), display small peaks belonging to (111) and (311) planes, and importantly, a very sharp and intense signal for the (220), or (110) plane. This thus confirms the significant prevalence of the (110) orientation on both polished and nucleation BDD surfaces, which is well in line with the EBSD mapping analysis discussed above. Moreover, the XRD rocking curve scans were acquired for the (110) plane of both the growth and nucleation sides, see Fig. S1(C, D). The curves are very broad (with FWHM $> 10°$) which indicates that the BDD surfaces are not sharply (110) textured. Besides, the relatively large grains (see Fig. 3) contribute to intense reflections, which cause the rocking curves not to have the character of a smooth line, but involve wide, irregular 'features'.

In the rest of the study, a smaller area of $100 \times 100\ \mu m^2$ localized in the upper right corner of the SEM/EBSD images of the polished growth BDD surface was selected for further investigation (see yellow dashed square in Fig. 2(B)). A detail of the EBSD orientation map for the chosen region, along with the oriented unit cells for several spots of interest, is provided in Fig. S2(A) in Supplementary material. In addition, Fig. S2(B) displays the corresponding topographic AFM image, where a notable difference in polishing 'efficiency' can be recognized as minor height variations of individual diamond grains. In particular, (110)-oriented crystals were smoothed down by polishing more effectively than the grains having (111) orientations, which protrude from the surface. Markedly, (111)-oriented crystals are harder to polish, even though they appear to be most heavily boron-doped (see below Section 3.2.1). Typically, though, higher impurity (boron) content leads to deteriorated wear resistance, as previously reported in [47]. Observed differences in wear resistance in the present study translated into local variations in the surface topography, however, the averaged surface roughness of the polished growth side of the polycrystalline BDD is very low at a level of *ca* 6 nm.

3.2. Raman analysis

Non-destructive Raman spectroscopy was used to assess the composition of the polished growth surface of the BDD electrode, which is most commonly subjected to electrochemical measurements. The same area previously examined by SEM/EBSD was analyzed by Raman mapping to find the correlation between on the one hand the morphology and crystal orientation and on the other hand the content of boron dopants and sp^2 carbon impurities. In particular, six different spots were identified in the EBSD orientation map, depicted in Fig. 4(A), and labelled with numbers 1 – 6 for easier description: 1, 2 – green, 3 – pink, and 4 – purple crystals leaning towards (110), (100), and (111) orientations, respectively; 5, 6 – twin boundaries.

3.2.1. Raman mapping of the polished growth surface

Fig. 4(B)–(D) presents a series of Raman spectral maps derived from (B) the diamond's zone-center phonon (ZCP) peak intensity, (C) the ZCP peak width, both indirectly related to the boron doping, and (D) the G peak intensity associated with the presence of non-diamond (sp^2) carbon. The position, width and intensity of the diamond's ZCP line (at $\sim$1330 cm^{-1} in Fig. 4(E)) are affected by the lattice structure, strain, and incorporated boron impurities. Particularly, with increasing boron content, the ZCP peak gradually decreased in intensity, broadened and

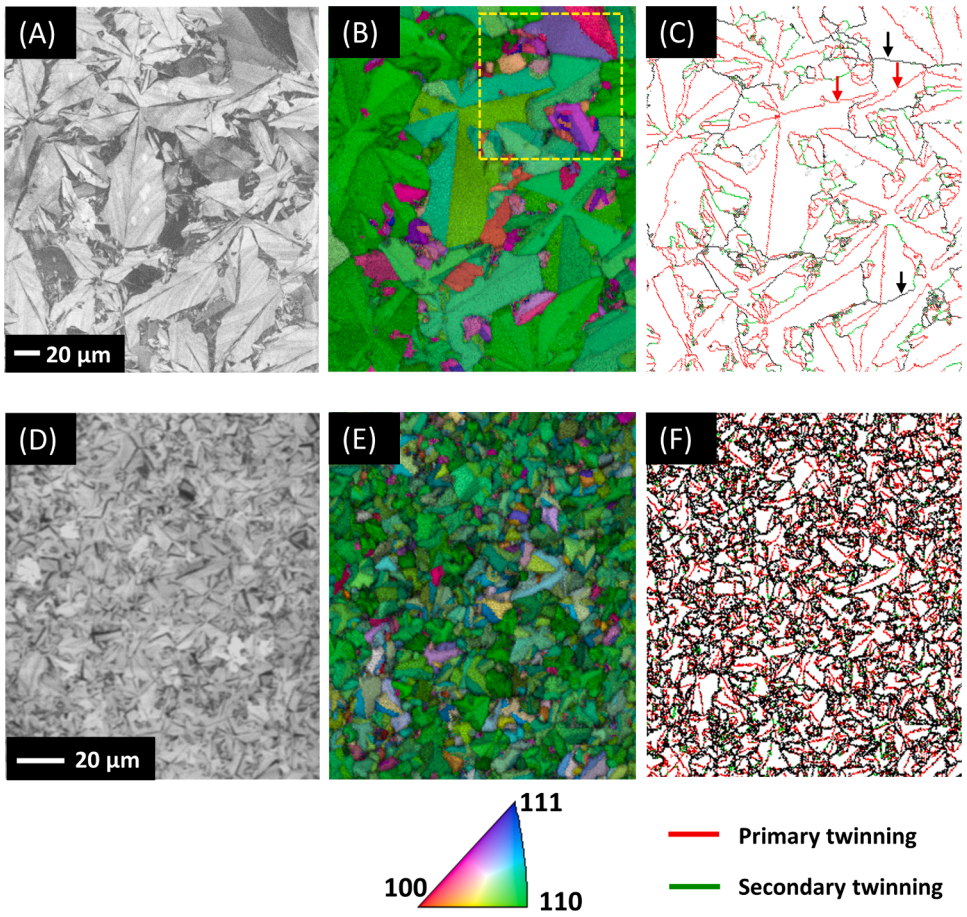

Fig. 2. (A, D) SEM images, (B, E) EBSD maps visualizing crystalline orientation (with a colour map), and (C, F) grain boundary maps acquired from the polished (A-C) growth surface and (D-F) nucleation surface of the free-standing, polycrystalline BDD electrode.

shifted toward a lower wavenumber [37,42,49]. This is demonstrated in Fig. 4(F), showing in detail the ZCP peak extracted from the Raman spectra acquired from the six selected locations within the investigated BDD region (see Section 3.2.2).

The Raman map of the ZCP line intensity in Fig. 4(B) correlates very well with the SEM image (see top right corner in Fig. 2(A)) and EBSD orientation map (Fig. 4(A)), and allows to identify all individual crystals. Notably, the line intensity in the map varies by almost a factor of 16 between the darker and brighter areas. The former ones, represented predominantly by spot 4 (purple crystal with (111) orientation) and spots 5 and 6 (twin boundaries), signalize lesser diamond (sp^3) content and simultaneously increased amount of boron and/or non-diamond (sp^2) carbon. In contrast, the brightest regions in the ZCP line intensity Raman map are mostly associated with (110)-faceted diamond crystals (e.g., spots 1 and 2 in Fig. 4(A)).

Fig. 4(C) depicts the Raman map constructed from the ZCP peak width, which can be used to indirectly determine the uptake of boron dopants within the investigated region [49]. However, it must be emphasized that the ZCP peak recorded by Raman spectroscopy is generally affected by the quantity of all defects, including the ones unrelated to boron incorporation [50]. Particularly, two types of areas of brighter contrast signalizing wider ZCP peaks, and thus possibly higher boron doping, were identified and were found complementary to the darker regions in the previous map constructed from the ZCP peak intensity (Fig. 4(B)): (i) spot 4 in the EBSD map representing a (111)-oriented crystal, which agrees with previous works reporting higher boron incorporation efficiency for the (111) crystals, compared to the (110)- and (100)-oriented facets [25–27], and (ii) twin (grain) boundaries, including spots 5 and 6. This also supports previous studies claiming on enrichment of boron atoms at twin boundaries [32,35] whose formation represents a highly effective coping mechanism for stress induced in the diamond lattice due to the impurity incorporation. Thus, our Raman mapping strongly indicates that boron atoms are non-uniformly distributed across the BDD electrode surface.

The third Raman map, shown in Fig. 4(D), was created based on the intensity of the G-band, a broad Raman signal centred at around 1547 cm^{-1}, whose origin is associated with the presence of sp^2 (non-diamond) carbon [51]. The highest intensity regions correspond to twin (grain) boundaries, where sp^2 carbon is, indeed, expected to reside [46]. Simultaneously, these areas are presumably enriched by incorporated boron atoms, as suggested by the Raman map shown in Fig. 4(C). Similar detection of predominant non-diamond carbon at sites showing increased boron concentration was made in [37].

3.2.2. *Raman spectra of the polished growth surface*

Individual Raman spectra recorded at the six different spots indicated in the EBSD map (see Fig. 4(A)) are displayed in Fig. 4(E). Naturally, the spectra differ depending on boron concentration ([B]) and presence or absence of sp^2 carbon phase. However, the common feature for all spectra is the diamond's ZCP line located in the range of 1327 – 1330 cm^{-1}, which is simultaneously the most pronounced signal. Magnification of this Raman peak is provided in Fig. 4(F) to clearly show its asymmetric and broadened line shape. As already mentioned, the ZCP line is downshifted from the expected position of a reference single-crystal undoped diamond (1332 cm^{-1}; indicated by the orange arrow in Fig. 4(F)). The differences in signal intensity and downshifts ranging

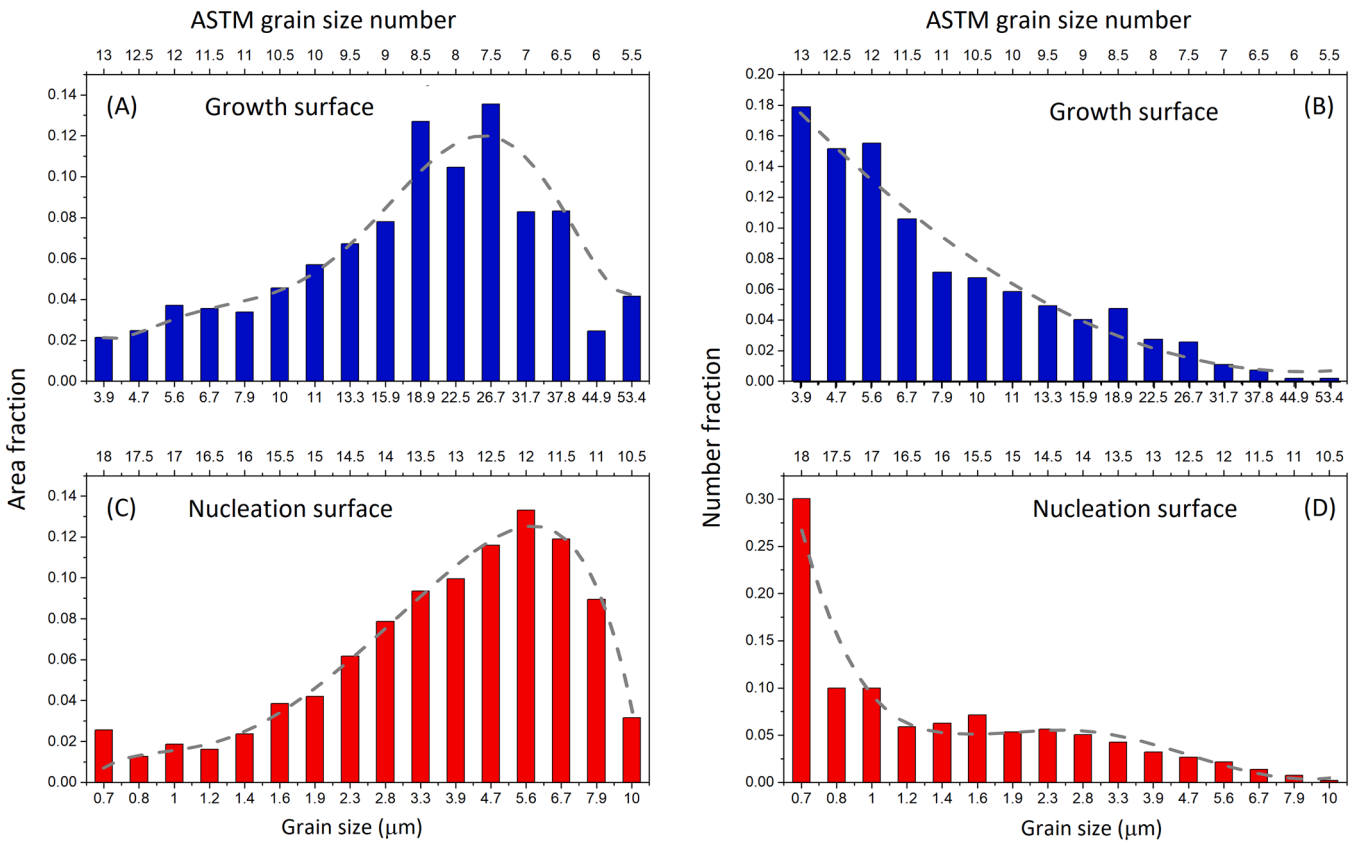

Fig. 3. Grain size distribution histograms for the polished (A, B) growth and (C, D) nucleation surface expressed by (A, C) area fraction and (B, D) number fraction. Data are plotted as a function of grain size (μm) and ASTM grain size number, respectively [48]. Grey dashed lines represent the fitting curves.

from 2 to 5 cm^{-1} imply surface areas of various boron doping level. This is supported by the [B] values determined using the Raman analysis tool thoroughly described in [52,53] and available at [54]. This fitting tool, developed for highly B-doped diamond (i.e., [B] $> 5 \times 10^{19}$ cm^{-3}), was used over the range from 1100 cm^{-1} to 1500 cm^{-1} as it is based on the analysis of two characteristic Raman peaks located at ~1200 cm^{-1} and ~1330 cm^{-1} attributed to the Fano-shaped maximum of phonon density of states and zone-centre phonon (ZCP) line of highly doped BDD, respectively. Importantly, both the position and the width of the ZCP (diamond) peak, which were proved to be proportional to the boron concentration [52], are considered in the fitting tool, among other parameters. Notably, for the selected spots in the investigated region of the polished growth surface, [B] spans over one order of magnitude from 7.0×10^{19} to 6.1×10^{20} atoms cm^{-3}; all values are listed in Fig. 4(E). This range accurately covers the average [B] value declared by the manufacturer (i.e., 3×10^{20} cm^{-3}).

For spots 1 – 3, also low-intensity peaks are present at ca 610, 925 and 1045 cm^{-1}, which are typical characteristics for BDD with boron doping levels in the range of 10^{18} – 10^{20} cm^{-3} [37,55], corresponding well with the boron estimation ([B]) above. Lastly, the G peak at 1547 cm^{-1} only arises in the Raman spectra acquired from twin boundaries, denoted as spots 5 and 6.

3.2.3. *Raman mapping of the cross-section area*

The exact same cross-section area, previously visualized using SEM and EBSD techniques (see Fig. 1), was subjected to Raman imaging. Fig. 5 displays two Raman maps which were created based on the intensity of the ZCP peak and the G band associated with the presence of sp^3 and sp^2 carbon, respectively. The mapping was not performed in one run but divided into smaller sections to avoid problems associated with overall cross-section non-uniformity and laser focusing. Note that the very edge (~10 μm) of the lower nucleation side was affected by the sample preparation procedure, which appears as a 'grey strip' in the Raman images, and thus no conclusions can be made on this area.

The acquired Raman maps demonstrate distinctive columnar growth of a polycrystalline diamond microstructure, which is consistent with the observations based on the SEM and EBSD images presented above in Section 3.1. Also, the Raman maps of the cross-section area are quite complementary. For example, bright areas of the highest ZCP peak intensity in Fig. 5(A) are simultaneously the least intense in Fig. 5(B), and vice versa. The ZCP peak intensity varies by a factor of ~24 across the cross-section area, which indicates heterogeneous character of the BDD material across the whole film thickness. Such variations and particularly a decrease in intensity can be ascribed to the incorporation of boron dopants and/or the presence of sp^2 carbon phase. This is consistent with the trends observed for the polished growth surface of the BDD electrode (see Section 3.2.2).

3.3. *Scanning electrochemical microscopy (SECM) measurements*

Next, the surface probe technique SECM, in its feedback mode, was employed to map the electrochemically active regions on the polished growth surface of the BDD electrode. The effect of topography on the obtained signals could be completely neglected as AFM measurements (see Fig. S2(B)) confirmed that the roughness of the investigated surface is at the nanometer scale. This allowed to conduct SECM mapping in constant-height mode, while using a Pt probe (10 μm tip diameter) in a solution of redox marker, 1 mM $FcMeOH^{+/0}$ (in 0.1 M KNO_3), with applied Pt tip potential of +0.5 V (vs. Ag/AgCl). The SECM map was recorded in the exact same area as the EBSD orientation and Raman

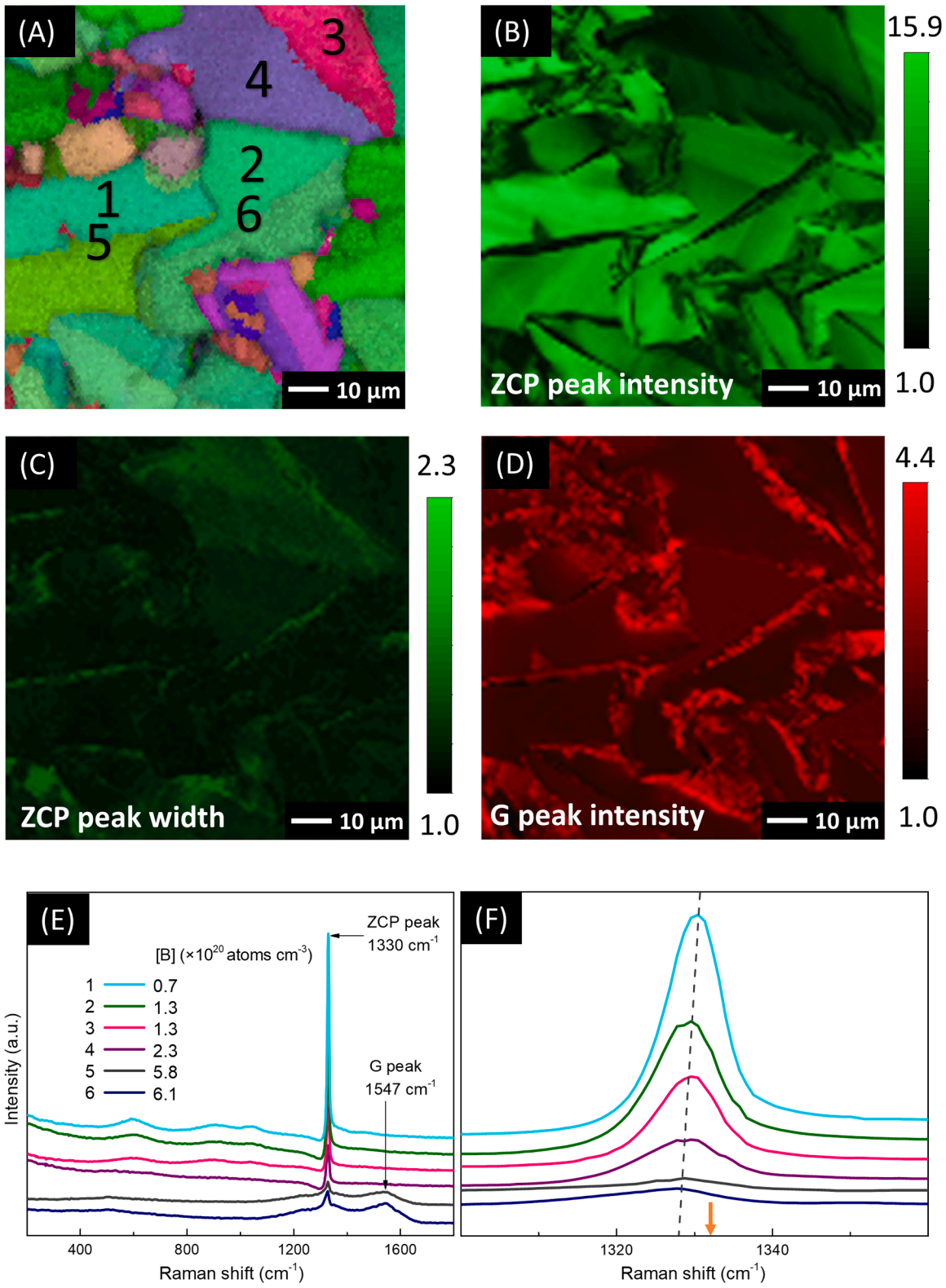

Fig. 4. (A) EBSD orientation map and (B)-(D) corresponding Raman maps of the polished growth surface of the free-standing, polycrystalline BDD electrode based on: (B) ZCP peak intensity, (C) ZCP peak width, and (D) G peak intensity. (E) Raman spectra recorded at the six different spots indicated in (A). (F) Respective zoomed-in ZCP diamond peaks where the dashed line follows a trend of peak downshift with increasing boron concentration. The orange arrow points to the Raman shift value (i.e., 1332 cm^{-1}) of an undoped single-crystal diamond sample.

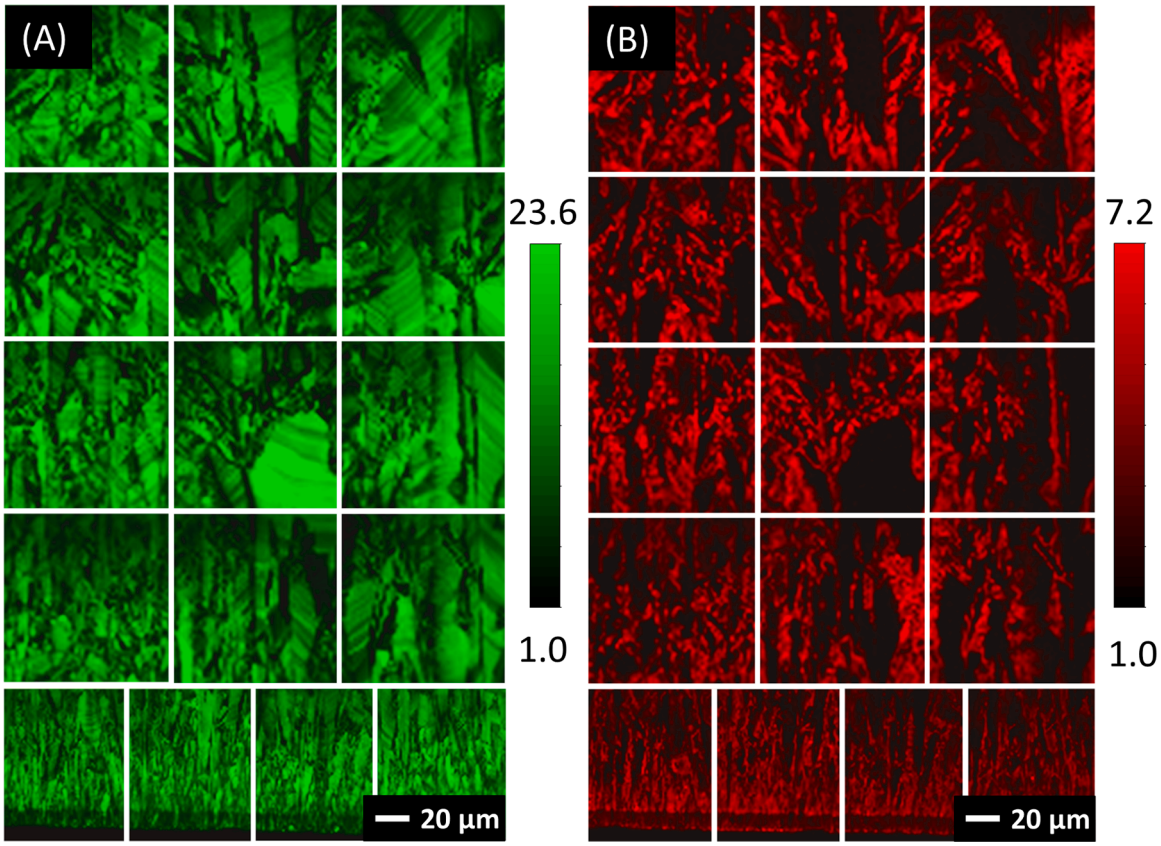

Fig. 5. Raman maps of the cross-section area of the BDD electrode based on the intensity of the (A) ZCP peak (sp^3 carbon) and (B) G peak (sp^2 carbon).

maps to draw correlation between local electrochemical activity and surface texture and composition, respectively.

The $FcMeOH^{+/0}$ redox probe was selected based on its outer-sphere character of electron transfer, which is insensitive to surface characteristics, including termination and extent of oxidation. The CV curve of $FcMeOH^{+/0}$ recorded on the polished growth surface, shown in Fig. S3 (A), displays a well-developed pair of redox peaks with a peak-to-peak separation value of 0.21 V. At the applied tip potential, oxidation of $FcMeOH^0$ to $FcMeOH^{1+}$ occurs at the Pt probe as verified, prior to the SECM measurements, by performing CV experiments; a representative CV is shown in Fig. S3(B). Also, information on the steady-state current, i_{ss} of 2.8 nA, was extracted from the CV. The scanned polycrystalline BDD substrate was kept under OCP conditions, thus no potential control was implemented.

The SECM map is shown in normalized current scale in Fig. 6(B) and displays non-uniform distribution of electrochemical activity across the investigated region with currents detected by the Pt probe (i_T) ranging from 2.7 nA to 5.5 nA. In general, a ratio of $i_T/i_{ss} < 1$ indicates the presence of non-conductive sites and in the recorded image, only one spot, denoted as "3" (around 15 µm in diameter) manifested such insulating property. This spot corresponds to a crystal with orientation leaning towards the (100) plane (see Fig. 6(A) and Fig. 2(B)). It was also the only spot providing negative feedback when probe approach curves were recorded, shown in Fig. 6(C), despite having estimated doping at the level of [B] $\sim 1 \times 10^{20}$ cm^{-3} (see Fig. 4(E)). This implies that the effect of crystal orientation may have a more dominant effect on the electrochemical response than the boron concentration. A similar remark was made in the work of Ivandini et al., where equally doped (100) and (111)-faceted single crystal BDD electrodes ([B] $\sim 4 \times 10^{20}$ cm^{-3}) were compared and hindered electron transfer kinetics and peaks of lower intensity were recorded for redox probes on the (100) facet, compared to the (111) crystal [15].

Nevertheless, the majority of the studied surface area showed $i_T/i_{ss} > 1$, and thus manifested electrochemically active and conductive behaviour, which was also confirmed by probe approach curves performed at the remaining five spots demonstrating positive feedback. Markedly, 'less pronounced' positive feedback was distinguished at spot 1, which corresponds to the (110)-oriented crystal having, according to Raman analysis (see Section 3.2.2), the lowest doping ([B] of 7×10^{19} cm^{-3}) among the investigated sites. A clear trend of gradual development of much more distinct positive feedback responses with increasing boron contents (see corresponding values in Fig. 4(E)) can be identified in Fig. 6(C), the only exception being spot 3, addressed above. However, when [B] exceeds 2×10^{20} cm^{-3}, i.e., metallic threshold [23,24], which is the case of spots 4, 5, and 6, the recorded probe approach curves become very comparable. This is presumably caused by the limited mass transfer rate of the redox marker to the Pt microprobe tip. As further evident from Fig. 6, the highest electrochemical activity was recorded at spot 4, i.e., the large crystal with (111) orientation and the highest boron concentration among the various grains (excluding the grain boundary regions). Local variations in electrochemical activity between different BDD crystal facets were evidenced by SECM-based techniques also in [28,37,42] and were correlated directly with differences in the local boron doping levels. It was postulated that the higher boron concentration yields increased density of states and electron transfer kinetics for outer-sphere redox probes [28].

Remarkably, twinning boundaries, exemplified by spots 5 and 6, showed no considerable increase in electrochemical activity even though the inter-grain regions are undoubtedly enriched by boron and sp^2 carbon (see Section 3.2). Apparently, such enrichment extracted from a series of Raman maps (see Fig. 4) and [B] estimation does not translate into enhanced electrochemical activity. This may be associated with the fact that Raman spectroscopy is sensitive to the overall amount of defect(s), i.e., also defects unrelated to boron incorporation into the

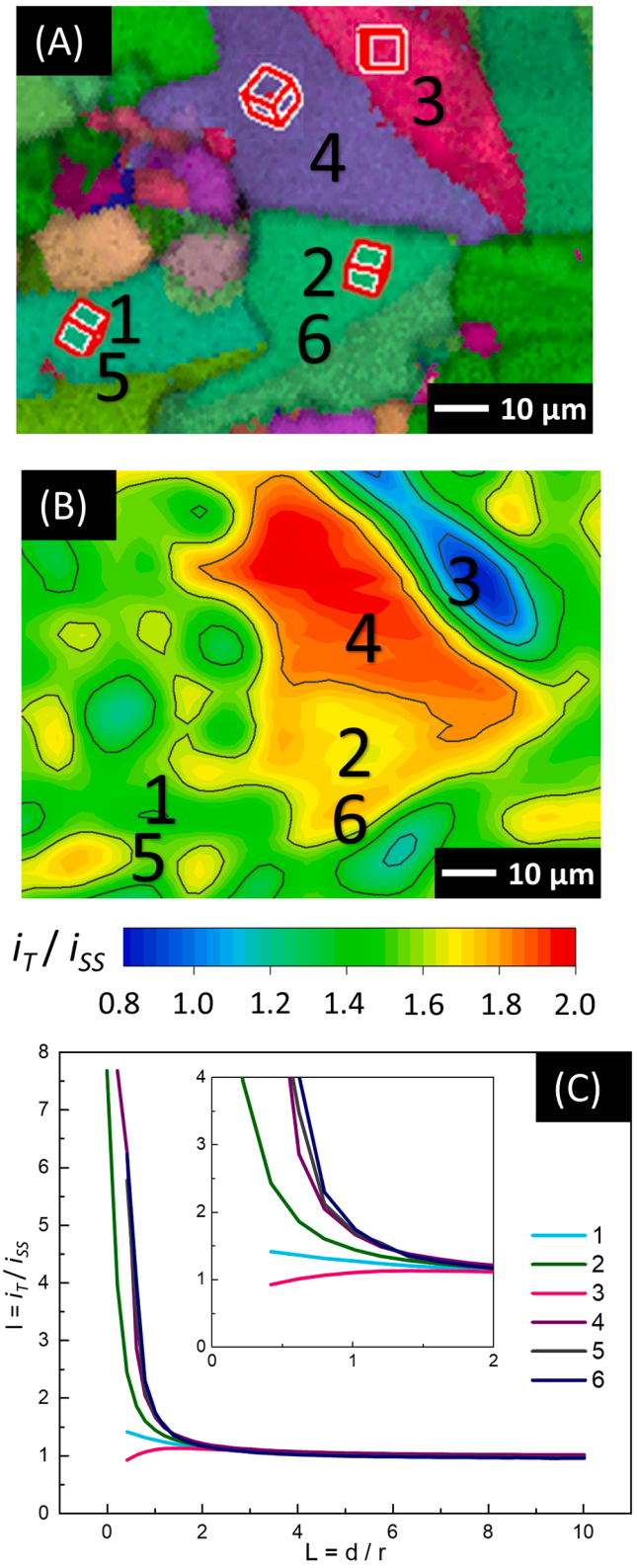

Fig. 6. (A) EBSD orientation map and (B) SECM map (100 × 80 µm^2) of the polished growth surface (same area) obtained with a 10 µm diameter Pt tip in 1 mM $FcMeOH^{+/0}$ (in 0.1 M KNO_3), with a tip potential of +0.5 V (vs. Ag/AgCl) and the BDD substrate kept under OCP. (C) Experimental probe approach curves recorded at the six different spots, as indicated by the numbers in (A) and (B).

diamond lattice can potentially affect the position, width and intensity of the ZCP diamond peak, as already mentioned in Section 3.1.1. Both electrically active and non-active boron atoms and other types of defects can contribute to the final ZCP lines displayed in Raman spectra [50]. Our observations are consistent with several previous works employing SECM-based techniques to probe the electrochemical activity of the BDD surfaces, in which no evidence confirming enhanced activity at grain boundaries was found [28,29,37,42].

The findings on the heterogeneity of the polished growth surface of the polycrystalline BDD electrode correlate well with our previous work, where SECM analysis was performed and we observed localized current variations and identified locations showing electrochemically active and non-active behaviour [22]. At that time, no further attempts to correlate these observations with EBSD or Raman maps were made. Now, we can convincingly propose that the non-uniform nature of the polycrystalline BDD electrode is largely dominated by the interplay of inhomogeneous boron doping level and crystal orientation of the individual grains. This claim is further supported by the SECM maps acquired for single-crystal BDD electrodes as reported in [22], which manifested uniform, conductive and electrochemically active nature, and no local variations in peak currents.

3.4. *Microstructure-electroactivity relationships*

Polycrystalline BDD is characterized by a columnar grain structure and, consequently, a highly non-uniform microstructure and composition is developed as a function of its thickness, which is schematically displayed in Fig. 7. The distinctive columnar structure was visualized by SEM images as well as by EBSD and Raman maps. In addition, for the cross-section area, EBSD revealed a mixture of crystal orientations and significant number of grain and twin boundaries, while Raman mapping demonstrated variations in intensities of ZCP (diamond) and G (sp^2 carbon) peaks. All three characterization techniques thus confirm heterogeneous character of the polycrystalline BDD material across the whole film thickness.

Such heterogeneity naturally also translated into the characteristics of the polished growth BDD surface, which was thoroughly investigated. The grains of various shapes and sizes (up to tens of µm in diameter) possessed predominantly (110) orientation. However, a portion of (100)- and (111)-oriented crystal facets was also identified. Different crystal orientations affected the boron uptake by the individual grains, while the highest incorporation efficiency was confirmed for the (111) crystals. Moreover, Raman spectroscopy detected elevated amount of boron dopants in the boundary regions, where also sp^2 carbon phase was predominantly present (see Fig. 7). However, no evidence of enhanced electrochemical responses was found for inter-grain regions despite their enrichment in boron and sp^2 carbon impurities; they are presumably residing in their electrically 'non-active forms'. In contrast, the most highly boron-doped (111) facet demonstrated the most pronounced electrochemical activity. Nevertheless, the intensity of the electrochemical responses cannot be ascribed only to localized boron doping levels. In particular, (100)-oriented grains, despite having average [B] of

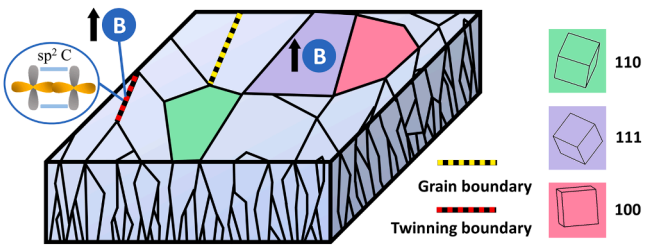

Fig. 7. Schematic representation of the investigated features on the free-standing, polycrystalline BDD electrode.

$\sim 1 \times 10^{20}$ cm^{-3}, showed poor electrochemical activity manifested by non-conductive (insulating) behaviour. This strongly suggests that crystal orientation is a leading factor controlling the electrochemical responses.

The crystal orientation of the individual BDD grains has been quite an overlooked parameter in the literature, while much more effort has been devoted into the investigation of other (however, still important) factors such as boron doping, sp^2 carbon content, and surface termination. Only recently, the significant effect of crystal orientation on the electrochemical behaviour of BDD electrodes has gained more attention. In several previous works, differences between crystal orientations were ascribed to different boron incorporation efficiency and resulting doping levels [26,29,42]. However, the more recent study comparing similarly doped (100)- and (111)-oriented BDD electrodes proved the superiority of the (111) facet over (100), which was associated with the different degrees of band bending and various thickness of space charge layer [15]. Further investigations at the atomic scale using low-temperature scanning tunnelling microscopy (STM) revealed that the dependence of the electrochemical activity of BDD electrodes on the crystal orientation originates from the boron-related deformation of the diamond lattice structure [53]. Specifically, graphitized domains related to boron incorporation were exclusively confirmed only in (111) facets, which could possibly explain their enhanced electrochemical activity, when compared to (100)-oriented crystals [56]. Besides, (113), (115) and (118)-oriented BDD electrodes of comparable [B] manifested different electrochemical responses, which was ascribed to the effect of crystal orientation and particularly to '(100)/(111) step' density [21].

All in all, boron atoms were found to be non-uniformly distributed over the polycrystalline BDD surface, but their presence was not always directly linked with greater electrochemical activity. Notably, next to boron concentration, crystallographic orientation has been identified as one of the dominating factors that largely govern the local electrochemical activity of the polycrystalline BDD electrodes.

This is expected to be true not only for thick, free-standing BDD electrodes but also for BDD thin films, composed of grains with various crystal orientations. However, one needs to be particularly careful to draw other parallel conclusions from the present study for thin films, often with submicron- or even nano-crystalline structures. This is because the scale of anisotropy and the resulting (doped) diamond's properties are primarily determined by the grain size, which in turn directs the amount of grain and twin boundaries. Markedly, as the diamond grains become smaller, the density of grain boundaries increases, and the non-diamond (sp^2) content becomes more prevalent [57,58]. Besides, a significant decline in doping efficiency was demonstrated for nanocrystalline BDD thin films, compared to the microcrystalline ones, which was ascribed to the fact that boron atoms incorporate in a significant manner in positions (such as grain boundaries) that do not contribute to the conductivity in the same way as boron dopants incorporated in the grains [58]. Therefore, all these factors and the interplay between them must be carefully considered in order to unravel the micro/nanostructure-electroactivity relationships within thin-film BDD.

4. Conclusion

Highly doped, free-standing polycrystalline BDD is a complex electrode material with distinct columnar structure and uneven distribution of boron dopants across the whole cross-section, which naturally manifest also in the characteristics and behaviour of the growth BDD surface. The individual grains showed considerably different electrochemical responses as a consequence of their various crystal orientations whose significant impact is not only related to varying boron uptake efficiency but also to the inherent structure of each individual facet. In our work, the highest doped (111)-oriented crystal demonstrated the highest electrochemical activity, as probed by SECM results. However, the averagely boron-doped (100) facet showed electrochemically inactive (insulating) nature. This therefore implies that the local electrochemical activity of the BDD surface is strongly grain dependent and the most significant factors governing the obtained electrochemical responses are the (previously often neglected) crystallographic orientation in addition to the boron doping level.

Besides, EBSD enabled to visualize the boundary regions at the polished growth surface, where increased content of boron atoms and sp^2 carbon was recognized by Raman mapping. However, such enrichment in impurities did not translate into enhanced electrochemical activity probed by SECM, which implies that boron atoms at the inter-grain spots are predominantly of electrically inactive nature.

Finally, it is essential to consider all relevant material characteristics (i.e., grain size distribution, presence of sp^2 carbon, boron content, surface finish and surface termination, and grain orientation) when working with, or designing, polycrystalline BDD electrodes, but also thin-film BDD and single-crystal BDD. This is particularly important for electrochemical applications where micro- to nano-meter scale phenomena are to be monitored or exploited, such as in neural interfacing or *in-vivo* analysis.

Declaration of competing interests

The authors declare that they have no known competing financial interests or personal relationships that could have appeared to influence the work reported in this paper.

Acknowledgements

Financial support from the Dutch Research Council (NWO) through the Open Technology Programme [project no. 16361] is gratefully acknowledged. The authors are thankful to Kees Kwakernaak and Ruud Hendrikx (Department of Materials Science and Engineering, Delft University of Technology, The Netherlands) for their help with the EBSD and XRD measurements, respectively, and to Mintres B.V. (The Netherlands) for providing the free-standing, polycrystalline BDD electrodes.

Supplementary materials

Supplementary material associated with this article can be found, in the online version, at doi:10.1016/j.actamat.2024.119671.

References

[1] S. Baluchová, A. Daňhel, H. Dejmková, V. Ostatná, M. Fojta, K. Schwarzová-Pecková, Recent progress in the applications of boron doped diamond electrodes in electroanalysis of organic compounds and biomolecules - A review, Anal. Chim. Acta 1077 (2019) 30–66, https://doi.org/10.1016/j.aca.2019.05.041.
[2] M. Yence, A. Cetinkaya, G. Ozcelikay, S.I. Kaya, S.A. Ozkan, Boron-doped diamond electrodes: Recent developments and advances in view of electrochemical drug sensors, Crit. Rev. Anal. Chem. 52 (2022) 1122–1138, https://doi.org/10.1080/10408347.2020.1863769.
[3] K. Sakanoue, A. Fiorani, C.I. Santo, G.Valenti Irkham, F. Paolucci, Y. Einaga, Boron-doped diamond electrode outperforms the state-of-the-art electrochemiluminescence from microbeads immunoassay, ACS Sens. 7 (2022) 1145–1155, https://doi.org/10.1021/acssensors.2c00156.
[4] Y. He, H. Lin, Z. Guo, W. Zhang, H. Li, W. Huang, Recent developments and advances in boron-doped diamond electrodes for electrochemical oxidation of organic pollutants, Sep. Purif. Technol. 212 (2019) 802–821, https://doi.org/10.1016/j.seppur.2018.11.056.
[5] O.M. Cornejo, M.F. Murrieta, L.F. Castañeda, J.L. Nava, Characterization of the reaction environment in flow reactors fitted with BDD electrodes for use in electrochemical advanced oxidation processes: A critical review, Electrochim. Acta 331 (2020) 135373, https://doi.org/10.1016/j.electacta.2019.135373.
[6] D. Suresh Babu, J.M.C. Mol, J.G. Buijnsters, Experimental insights into anodic oxidation of hexafluoropropylene oxide dimer acid (GenX) on boron-doped diamond anodes, Chemosphere 288 (2022) 132417, https://doi.org/10.1016/j.chemosphere.2021.132417.

[7] S. Lips, S.R. Waldvogel, Use of boron-doped diamond electrodes in electro-organic synthesis, ChemElectroChem 6 (2019) 1649–1660, https://doi.org/10.1002/celc.201801620.

[8] C. Guo, J. Zheng, H. Deng, P. Shi, G. Zhao, Photoelectrocatalytic interface of boron-doped diamond: Modification, functionalization and environmental applications, Carbon 175 (2021) 454–466, https://doi.org/10.1016/j.carbon.2020.12.027.

[9] S. Yu, N. Yang, S. Liu, X. Jiang, Diamond supercapacitors: Progress and perspectives, Curr. Opin. Solid State Mater. Sci. 25 (2021) 100922, https://doi.org/10.1016/j.cossms.2021.100922.

[10] N. Yang, S. Yu, J.V. Macpherson, Y. Einaga, H. Zhao, G. Zhao, G.M. Swain, X. Jiang, Conductive diamond: synthesis, properties, and electrochemical applications, Chem. Soc. Rev. 48 (2019) 157–204, https://doi.org/10.1039/C7CS00757D.

[11] S. Yu, S. Liu, X. Jiang, N. Yang, Recent advances on electrochemistry of diamond related materials, Carbon 200 (2022) 517–542, https://doi.org/10.1016/j.carbon.2022.09.044.

[12] Z. Deng, R. Zhu, L. Ma, K. Zhou, Z. Yu, Q. Wei, Diamond for antifouling applications: a review, Carbon 196 (2022) 923–939, https://doi.org/10.1016/j.carbon.2022.05.015.

[13] S. Baluchová, A. Taylor, V. Mortet, S. Sedláková, L. Klimša, J. Kopeček, O. Hák, K. Schwarzová-Pecková, Porous boron doped diamond for dopamine sensing: Effect of boron doping level on morphology and electrochemical performance, Electrochim. Acta 327 (2019) 135025, https://doi.org/10.1016/j.electacta.2019.135025.

[14] K. Schwarzová-Pecková, J. Vosáhlová, J. Barek, I. Šloufová, E. Pavlova, V. Petrák, J. Zavázalová, Influence of boron content on the morphological, spectral, and electroanalytical characteristics of anodically oxidized boron-doped diamond electrodes, Electrochim. Acta 243 (2017) 170–182, https://doi.org/10.1016/j.electacta.2017.05.006.

[15] T.A. Ivandini, T. Watanabe, T. Matsui, Y. Ootani, S. Iizuka, R. Toyoshima, H. Kodama, H. Kondoh, Y. Tateyama, Y. Einaga, Influence of surface orientation on electrochemical properties of boron-doped diamond, J. Phys. Chem. C 123 (2019) 5336–5344, https://doi.org/10.1021/acs.jpcc.8b10406.

[16] S. Baluchová, A. Mamaloukou, R.H.J.M. Koldenhof, J.G. Buijnsters, Modification-free boron-doped diamond as a sensing material for direct and reliable detection of the antiretroviral drug nevirapine, Electrochim. Acta 450 (2023) 142238, https://doi.org/10.1016/j.electacta.2023.142238.

[17] Z. Liu, A.F. Sartori, J.G. Buijnsters, Role of sp^2 carbon in non-enzymatic electrochemical sensing of glucose using boron-doped diamond electrodes, Electrochem. Commun. 130 (2021) 107096, https://doi.org/10.1016/j.elecom.2021.107096.

[18] J. Anaya, S. Rossi, M. Alomari, E. Kohn, L. Tóth, B. Pécz, K.D. Hobart, T. J. Anderson, T.I. Feygelson, B.B. Pate, M. Kuball, Control of the in-plane thermal conductivity of ultra-thin nanocrystalline diamond films through the grain and grain boundary properties, Acta Mater. 103 (2016) 141–152, https://doi.org/10.1016/j.actamat.2015.09.045.

[19] J.V. Macpherson, A practical guide to using boron doped diamond in electrochemical research, Phys. Chem. Chem. Phys. 17 (2015) 2935–2949, https://doi.org/10.1039/C4CP04022H.

[20] M. Zelenský, J. Fischer, S. Baluchová, L. Klimša, J. Kopeček, M. Vondráček, L. Fekete, J. Eidenschink, F.M. Matysik, S. Mandal, O.A. Williams, M. Hromadová, V. Mortet, K. Schwarzová-Pecková, A. Taylor, Chem-mechanical polishing influenced morphology, spectral and electrochemical characteristics of boron doped diamond, Carbon 203 (2023) 363–376, https://doi.org/10.1016/j.carbon.2022.11.069.

[21] A. Taylor, S. Baluchová, L. Fekete, L. Klimša, J. Kopeček, D. Šimek, M. Vondráček, L. Míka, J. Fischer, K. Schwarzová-Pecková, V. Mortet, Growth and comparison of high-quality MW PECVD grown B doped diamond layers on {118}, {115} and {113} single crystal diamond substrates, Diam. Relat. Mater. 123 (2022) 108815, https://doi.org/10.1016/j.diamond.2021.108815.

[22] Z. Liu, S. Baluchová, A.F. Sartori, Z. Li, Y. Gonzalez-Garcia, M. Schreck, J. G. Buijnsters, Heavily boron-doped diamond grown on scalable heteroepitaxial quasi-substrates: A promising single crystal material for electrochemical sensing applications, Carbon 201 (2023) 1229–1240, https://doi.org/10.1016/j.carbon.2022.10.023.

[23] M. Bernard, A. Deneuville, P. Muret, Non-destructive determination of the boron concentration of heavily doped metallic diamond thin films from Raman spectroscopy, Diam. Relat. Mater. 13 (2004) 282–286, https://doi.org/10.1016/j.diamond.2003.10.051.

[24] J.P. Lagrange, A. Deneuville, E. Gheeraert, Activation energy in low compensated homoepitaxial boron-doped diamond films, Diam. Relat. Mater. 7 (1998) 1390–1393, https://doi.org/10.1016/S0925-9635(98)00225-8.

[25] Y.V. Pleskov, Y.E. Evstefeeva, M.D. Krotova, V.P. Varnin, I.G. Teremetskaya, Synthetic semiconductor diamond electrodes: Electrochemical behaviour of homoepitaxial boron-doped films orientated as (111), (110), and (100) faces, J. Electroanal. Chem. 595 (2006) 168–174, https://doi.org/10.1016/j.jelechem.2006.07.010.

[26] K. Ushizawa, K. Watanabe, T. Ando, I. Sakaguchi, M. Nishitani-Gamo, Y. Sato, H. Kanda, Boron concentration dependence of Raman spectra on {100} and {111} facets of B-doped CVD diamond, Diam. Relat. Mater. 7 (1998) 1719–1722, https://doi.org/10.1016/S0925-9635(98)00296-9.

[27] T. Kondo, Y. Einaga, B.V. Sarada, T.N. Rao, D.A. Tryk, A. Fujishima, Homoepitaxial single-crystal boron-doped diamond electrodes for electroanalysis, J. Electrochem. Soc. 149 (2002) E179, https://doi.org/10.1149/1.1471548.

[28] H.V. Patten, S.C.S. Lai, J.V. Macpherson, P.R. Unwin, Active sites for outer-sphere, inner-sphere, and complex multistage electrochemical reactions at polycrystalline boron-doped diamond electrodes (pBDD) revealed with scanning electrochemical cell microscopy (SECCM), Anal. Chem. 84 (2012) 5427–5432, https://doi.org/10.1021/ac3010555.

[29] N.R. Wilson, S.L. Clewes, M.E. Newton, P.R. Unwin, J.V. Macpherson, Impact of grain-dependent boron uptake on the electrochemical and electrical properties of polycrystalline boron doped diamond electrodes, J. Phys. Chem. B 110 (2006) 5639–5646, https://doi.org/10.1021/jp0547616.

[30] T. Ando, K. Asai, J. Macpherson, Y. Einaga, T. Fukuma, Y. Takahashi, Nanoscale reactivity mapping of a single-crystal boron-doped diamond particle, Anal. Chem. 93 (2021) 5831–5838, https://doi.org/10.1021/acs.analchem.1c00053.

[31] J.E. Butler, I. Oleynik, A mechanism for crystal twinning in the growth of diamond by chemical vapour deposition, Philos. Trans. Royal Soc. A 366 (2008) 295–310, https://doi.org/10.1098/rsta.2007.2152.

[32] Y.G. Lu, S. Turner, J. Verbeeck, S.D. Janssens, P. Wagner, K. Haenen, G. Van Tendeloo, Direct visualization of boron dopant distribution and coordination in individual chemical vapor deposition nanocrystalline B-doped diamond grains, Appl. Phys. Lett. 101 (2012), https://doi.org/10.1063/1.4738885.

[33] A. Boussadi, A. Tallaire, O. Brinza, M.A. Pinault-Thaury, J. Achard, Thick heavily boron doped CVD diamond films homoepitaxially grown on (111)-oriented substrates, Diam. Relat. Mater. 79 (2017) 108–111, https://doi.org/10.1016/j.diamond.2017.08.017.

[34] C. Wild, R. Kohl, N. Herres, W. Müller-Sebert, P. Koidl, Oriented CVD diamond films: twin formation, structure and morphology, Diam. Relat. Mater. 3 (1994) 373–381, https://doi.org/10.1016/0925-9635(94)90188-0.

[35] K.E. Bennet, K.H. Lee, J.N. Kruchowski, S..Y. Chang, M.P. Marsh, A.A. Van Orsow, A. Paez, F.S. Manciu, Development of conductive boron-doped diamond electrode: A microscopic, spectroscopic, and voltammetric study, Materials 6 (2013) 5726–5741, https://doi.org/10.3390/ma6125726.

[36] A. Zieliński, R. Bogdanowicz, J. Ryl, L. Burczyk, K. Darowicki, Local impedance imaging of boron-doped polycrystalline diamond thin films, Appl. Phys. Lett. 105 (2014) 131908, https://doi.org/10.1063/1.4897346.

[37] S. Szunerits, M. Mermoux, A. Crisci, B. Marcus, P. Bouvier, D. Delabouglise, J. P. Petit, S. Janel, R. Boukherroub, L. Tay, Raman imaging and Kelvin probe microscopy for the examination of the heterogeneity of doping in polycrystalline boron-doped diamond electrodes, J. Phys. Chem. B 110 (2006) 23888–23897, https://doi.org/10.1021/jp064429.

[38] K.B. Holt, A.J. Bard, Y. Show, G.M. Swain, Scanning electrochemical microscopy and conductive probe atomic force microscopy studies of hydrogen-terminated boron-doped diamond electrodes with different doping levels, J. Phys. Chem. B 108 (2004) 15117–15127, https://doi.org/10.1021/jp048222x.

[39] K. Honda, T. Noda, M. Yoshimura, K. Nakagawa, A. Fujishima, Microstructural heterogeneity for electrochemical activity in polycrystalline diamond thin films observed by electrogenerated chemiluminescence imaging, J. Phys. Chem. B 108 (2004) 16117–16127, https://doi.org/10.1021/jp040395z.

[40] J.W. Steeds, A. Gilmore, S. Charles, P. Heard, B. Howarth, J.E. Butler, Use of novel methods for the investigation of the boron distribution in CVD diamond, Acta Mater. 47 (1999) 4025–4030, https://doi.org/10.1016/S1359-6454(99)00262-1.

[41] A. Zielinski, M. Cieslik, M. Sobaszek, R. Bogdanowicz, K. Darowicki, J. Ryl, Multifrequency nanoscale impedance microscopy (m-NIM): A novel approach towards detection of selective and subtle modifications on the surface of polycrystalline boron-doped diamond electrodes, Ultramicroscopy 199 (2019) 34–45, https://doi.org/10.1016/j.ultramic.2019.01.004.

[42] H.V. Patten, K.E. Meadows, L.A. Hutton, J.G. Iacobini, D. Battistel, K. McKelvey, A. W. Colburn, M.E. Newton, J.V. Macpherson, P.R. Unwin, Electrochemical mapping reveals direct correlation between heterogeneous electron-transfer kinetics and local density of states in diamond electrodes, Angew. Chem., Int. Ed. 51 (2012) 7002–7006, https://doi.org/10.1002/anie.201203057.

[43] T. Liu, D. Raabe, W. Mao, S. Zaefferer, Microtexture and grain boundaries in freestanding CVD diamond films: Growth and twinning mechanisms, Adv. Funct. Mater. 19 (2009) 3880–3891, https://doi.org/10.1002/adfm.200901231.

[44] C. Wild, N. Herres, P. Koidl, Texture formation in polycrystalline diamond films, J. Appl. Phys. 68 (1990) 973–978, https://doi.org/10.1063/1.346663.

[45] D.Q. Liu, C.H. Chen, D. Perry, G. West, S.J. Cobb, J.V. Macpherson, P.R. Unwin, Facet-resolved electrochemistry of polycrystalline boron-doped diamond electrodes: Microscopic factors determining the solvent window in aqueous potassium chloride solutions, ChemElectroChem 5 (2018) 3028–3035, https://doi.org/10.1002/celc.201800770.

[46] M. Mohr, L. Daccache, S. Horvat, K. Brühne, T. Jacob, H.J. Fecht, Influence of grain boundaries on elasticity and thermal conductivity of nanocrystalline diamond films, Acta Mater. 122 (2017) 92–98, https://doi.org/10.1016/j.actamat.2016.09.042.

[47] J.G. Buijnsters, M. Tsigkourakos, T. Hantschel, F.O.V. Gomes, T. Nuytten, P. Favia, H. Bender, K. Arstila, J.P. Celis, W. Vandervorst, Effect of boron doping on the wear behavior of the growth and nucleation surfaces of micro- and nanocrystalline diamond films, ACS Appl. Mater. Interfaces 8 (2016) 26381–26391, https://doi.org/10.1021/acsami.6b08083.

[48] ASTM E112 - 96 (2004). Standard test methods for determining average grain size.

[49] K. Srimongkon, S. Ohmagari, Y. Kato, V. Amornkitbamrung, S.I. Shikata, Boron inhomogeneity of HPHT-grown single-crystal diamond substrates: confocal micro-Raman mapping investigations, Diam. Relat. Mater. 63 (2016) 21–25, https://doi.org/10.1016/j.diamond.2015.09.014.

[50] A. Taylor, P. Ashcheulov, P. Hubík, Z. Weiss, L. Klimša, J. Kopeček, J. Hrabovsky, M. Veis, J. Lorinčík, I. Elantyev, V. Mortet, Comparative determination of atomic boron and carrier concentration in highly boron doped nano-crystalline diamond, Diam. Relat. Mater. 135 (2023) 109837, https://doi.org/10.1016/j.diamond.2023.109837.

[51] A. Merlen, J.G. Buijnsters, C. Pardanaud, A guide to and review of the use of multiwavelength Raman spectroscopy for characterizing defective aromatic carbon solids: from graphene to amorphous carbons, Coatings 7 (2017) 153, https://doi.org/10.3390/coatings7100153.

[52] V. Mortet, Z.V. Živcová, A. Taylor, M. Davydová, O. Frank, P. Hubík, J. Lorincik, M. Aleshin, Determination of atomic boron concentration in heavily boron-doped diamond by Raman spectroscopy, Diam. Relat. Mater. 93 (2019) 54–58, https://doi.org/10.1016/j.diamond.2019.01.028.

[53] V. Mortet, I. Gregora, A. Taylor, N. Lambert, P. Ashcheulov, Z. Gedeonova, P. Hubik, New perspectives for heavily boron-doped diamond Raman spectrum analysis, Carbon 168 (2020) 319–327, https://doi.org/10.1016/j.carbon.2020.06.075.

[54] Raman analysis tool: https://ramantool.pythonanywhere.com/ (accessed 02-06-2023).

[55] A. Crisci, M. Mermoux, B. Saubat-Marcus, Deep ultra-violet Raman imaging of CVD boron-doped and non-doped diamond films, Diam. Relat. Mater. 17 (2008) 1207–1211, https://doi.org/10.1016/j.diamond.2008.01.025.

[56] F.C.I. Catalan, L.T. Anh, J. Oh, E. Kazuma, N. Hayazawa, N. Ikemiya, N. Kamoshida, Y. Tateyama, Y. Einaga, Y. Kim, Localized graphitization on diamond surface as a manifestation of dopants, Adv. Mater. 33 (2021) 2103250, https://doi.org/10.1002/adma.202103250.

[57] O.A. Williams, A. Kriele, J. Hees, M. Wolfer, W. Müller-Sebert, C.E. Nebel, High Young's modulus in ultra thin nanocrystalline diamond, Chem. Phys. Lett. 495 (2010) 84–89, https://doi.org/10.1016/j.cplett.2010.06.054.

[58] P.W. May, W.J. Ludlow, M. Hannaway, P.J. Heard, J.A. Smith, K.N. Rosser, Raman and conductivity studies of boron-doped microcrystalline diamond, facetted nanocrystalline diamond and cauliflower diamond films, Diam. Relat. Mater. 17 (2008) 105–117, https://doi.org/10.1016/j.diamond.2007.11.005.